Nonaqueous TiO_2 Nanoparticle Synthesis: a Versatile Basis for the Fabrication of Self-Supporting, Transparent, and UV-Absorbing Composite Films

Dorota Koziej,* Fabian Fischer, Niklaus Kränzlin, Walter R. Caseri, and Markus Niederberger*

Department of Materials, ETH Zürich, Wolfgang Pauli Strasse 10, CH-8093 Zürich, Switzerland

ABSTRACT A successful strategy to obtain self-supporting (100 μm), UV-absorbing, and, in the visible region, highly transparent TiO_2–poly(methyl methacrylate) (PMMA) films was developed. The 15 nm large anatase TiO_2 nanocrystals were prepared in a nonaqueous sol–gel approach involving the mixing of $Ti(O^iPr)_4$ and benzyl alcohol. The surfaces of the resulting particles were modified with minute amounts of organic ligands in order to make the particles easily dispersible in nonpolar media like xylene and dichloromethane and compatible with PMMA, a polymer of high optical transparency and considerable technical importance. The empirical optimization process of composite fabrication was supplemented by fundamental studies of the crystallization and growth mechanism of anatase particles in a nonaqueous medium. After the preparation of corresponding nanocomposites, the materials were investigated with respect to their UV absorption capability, optical transparency in the visible-wavelength region, and photodegradation.

KEYWORDS: UV-absorbing nanocomposite • titanium dioxide • PMMA • nonaqueous synthesis • self-supporting films

INTRODUCTION

Organic–inorganic composites for applications in optics, photonics, and information technology must exhibit a highly innovative ensemble of properties (1–4). Therefore, titanium dioxide–polymer nanocomposite materials with high refractive index and optical transparency are highly interesting for optically transparent UV filter or highly refractive fiber coatings (5). Crucial for their development is the fabrication of homogeneous composites with nanoparticles smaller than 40 nm. Such particles hardly scatter any visible light and, thus, retain optical transparency of the polymer matrix. Moreover, because of their high refractive index (2.45–2.9 dependent on the crystallographic modification) and UV absorption (indirect band gap of 3.2 eV), they significantly improve the optical properties of the matrix, giving an opportunity to engineer linear and nonlinear optical properties and to prepare different types of photonic materials like fibers, optical modulators, or optical switches at high frequencies (3, 5). The refractive index of the nanocomposites can be tuned, or the unique ultrafast nonlinear optical response can be induced by changing, e.g., the concentration of the nanoparticles in the matrix, their size, their surface modification, and the dielectric properties of the polymer matrix (3, 6–10). Titanium dioxide–polymer nanocomposites found also special application in optical data storage, in which nanoparticles are used for obtaining a higher refractive index contrast of the volume holograms compared to those in pure organic materials (11, 12).

Because of the extensive literature available, we will only briefly describe the state of the art in the fabrication of nanocomposites but then outline in more detail the challenges in the production of the TiO_2 nanocrystal–polymer composites. In general, two strategies are applied: (a) in situ, which comprise either the synthesis of inorganic particles in the polymer matrix (13, 14), the polymerization of the organic matrix around the inorganic nanoparticles (12, 15, 16), or sol–gel polymerization (10, 17, 18); (b) ex situ synthesis of naonoparticles and their direct incorporation into the polymer matrix by mechanical blending, polymer melt intercalation, or solvent processing (6, 19, 20).

The first strategy enables control of the organic–inorganic interaction at the molecular scale and results in highly homogeneous nanocomposites (17). For instance, titanium alkoxide mixed with an organic monomer during in situ polymerization undergoes simultaneous hydrolysis and condensation reactions, resulting in monodispersed composites (9, 10, 21). Therefore, the usage of this procedure is more or less restricted to the application of polymers that are soluble in the aqueous reaction medium of the particle synthesis, however, most of the technically relevant polymers are insoluble in water. Furthermore, it was reported that because obtained inorganic domains are amorphous and in order to enhance their crystallinity, a post-treatment of the composites following a complex protocol with control

* To whom correspondence should be addressed. E-mail: dorota.koziej@mat.ethz.ch. (D.K.), markus.niederberger@mat.ethz.ch (M.N.). Fax: +41446321545.

Received for review January 28, 2009 and accepted April 13, 2009

DOI: 10.1021/am9000584

over several parameters is required (8, 9, 21−23). In addition, undesired species in the composites coming either from the side products of nanoparticle synthesis or from the polymerization step may be produced. The compatibility of bare TiO_2 particles with those relatively hydrophobic polymers is also impeded by the hydrophilic nature of bare TiO_2. These make the in situ process complex and limit its application on an industrial scale (17). Interestingly, homogeneity of the composites is considered to be the most important advantage of the in situ method and, at the same time, inhomogenity is the most remarkable drawback of the ex situ approach. Nevertheless, the second strategy provides the flexibility of choosing inorganic and organic building blocks with well-defined properties and thus the possibility of tuning the properties of the final nanocomposite. The availability of reliable synthesis protocols, leading to nanocrystals being uniform in composition, size, shape, and surface chemistry, is essential for practical application of the ex situ approach. In this respect, the nonaqueous synthesis route is beneficial, delivering highly crystalline TiO_2 nanoparticles with narrow size distribution and with a weak tendency toward aggregation (24−26). Furthermore, a crucial factor determining the quality of the composites obtained via an ex situ route is control over the interaction between the polymer matrix and the nanoparticles' surface. Organic groups attached to the surface of nanoparticles after the nonaqueous synthesis prevent agglomeration and provide a tool to adjust the surface polarity to both the polar and apolar media (27). For instance, it was shown that (a) even minute amounts of stabilizers allow the preparation of stable dispersions of ZrO_2 in a nonpolar medium (28), (b) in situ functionalization tailors the solubility properties of nanocrystalline titania in a nonpolar medium (29), and (c) ligand-free TiO_2 nanoparticles can be prepared and their further controlled postfunctionalization enables the preparation of stable dispersions in a water environment (30). The selected examples demonstrate the great versatility of the nonaqueous synthesis route and justify the choice of this method.

In the present report, we focus on the nonaqueous synthesis of TiO_2 nanoparticles and their ex situ incorporation into a poly(methyl methacrylate) (PMMA) polymer matrix by solvent processing. This work is three-fold.

First, we investigate the crystallization and growth of TiO_2 particles in benzyl alcohol in the presence of minute amounts of silanes. Although the nonaqueous synthesis routes give access to uniform anatase TiO_2 nanocrystals with a wide variety of sizes (25), in this paper we focus on the fabrication of particles larger than 10 nm but smaller than 50 nm. The motivation of this choice is in the optical and photocatalytic properties of the nanoparticles. According to the Mie theory, nanoparticles smaller than 50 nm hardly scatter any visible light and, thus, retain optical transparency. However, 10-nm-sized particles are still large enough to avoid the quantum confinement effects (31). It was shown that the photocatalytic activity of anatase TiO_2 strongly increases with a decrease in the particle size (31). This activity promotes photodegradation of the PMMA matrix in the composite film and leads to transparency losses (32). The photodegradation process can be manifested by discoloration through darkening or yellowing of the polymer (33, 34). Therefore, we expect to obtain weaker photocatalytic effects with larger crystals, which will inhibit photodegradation of the polymer matrix in the composite film. As described elsewhere (35), it could be shown that in situ functionalization of nanocrystalline titania in a nonaqueous medium leads to good dispersion behavior. However, the particles obtained there were smaller than 10 nm and not fulfilling our size requirements. This was the main driving force to adopt in situ functionalization to the solvothermal reaction with alkoxide as the precursor. In our synthesis procedure, we in situ functionalize the surface of TiO_2 nanoparticles in benzyl alcohol in the autoclave.

Second, we investigate the dispersibility of the as-prepared TiO_2 nanoparticles in a nonpolar medium, i.e., in xylene and dichloromethane.

Third, we present that postfunctionalization renders the particles compatible with the polymer, offering an attractive ex situ approach for the fabrication of self-supporting, optically transparent, but UV-absorbing nanocomposite films. Moreover, the composites exhibit high photostability, making them attractive for use in commercial applications.

RESULTS AND DISCUSSION

Organic Reaction Products. The final reaction solution was subjected to detailed NMR analysis to elucidate the influence of the additives on the reaction mechanism by retroanalysis. It was reported that the reaction of titanium(IV) tetraisopropoxide in benzyl alcohol at 200 °C proceeds by a two-step process involving ligand exchange and ether elimination. The liquid product of the reaction contained benzyl ether and isopropyl ether (29). We slightly decreased the reaction temperature down to 190 °C, corresponding to the boiling point of 3-(trimethoxysilyl)propyl methacrylate (MPS; see below), but qualitatively the organic products remained unchanged (NMR spectra and peak assignments are included in the Supporting Information). The organic phase was basically the same whether or not silanes were present; i.e., the formation of TiO_2 follows in all cases the conventional ether elimination route.

Crystallization and Growth of TiO_2 (Anatase). In the surfactant/silane-free synthesis of metal oxide nanoparticles, the organic solvents play a crucial role in determining the particle size, shape, and size distribution (29). X-ray diffraction (XRD) patterns (see the Supporting Information) and transmission electron microscopy (TEM) images (Figure 1) clearly identify the particles obtained in this work as highly crystalline anatase without another crystal modification of TiO_2 (25, 29). On the TEM images, the particle sizes lie typically in the range 10−20 nm, which is in agreement with the mean crystal size value of 14 nm estimated by Scherrer's equation of the (101) peak from the X-ray diffractogram. The well-resolved (101) lattice planes with a *d* spacing of 3.385 Å are also denoted in the high-resolution TEM (HRTEM) micrograph (inset).

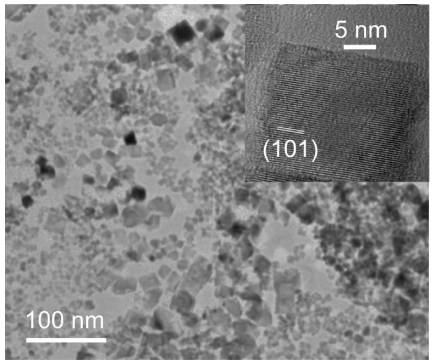

FIGURE 1. TEM and HRTEM (in inset) images of particles obtained from the reaction without silanes.

The presence of silanes during TiO_2 particle formation did not influence the size of the crystals significantly. The calculated average sizes of differently prepared TiO_2 nanoparticles are summarized in Table 1. In all cases, the particles have a plateletlike shape, with the side length ranging from 7 to 23 nm and a thickness of 5 nm (Figures 1−3). Figure 3 (inset top) shows the edge of a single TiO_2 platelet that is about 15 nm long and 5 nm thick. The high crystallinity of the particles is confirmed by HRTEM analysis. The corresponding power spectrum (fast Fourier transform: inset bottom) points to the single-crystalline nature of the TiO_2 particles. Analysis of the distances and angles of the array of discrete spots in the power spectrum reveals that the displayed TiO_2 crystallite is in the [010] zone-axis orientation.

In general, an additive can interact in many ways with the starting materials and the reaction intermediates (36, 37). In the following, we discuss, as an example, the influence of MPS on the crystallization and growth of anatase particles. The variation of the reaction time provides a hint about the crystallization mechanism of the nanoparticles. The decrease of the reaction time from 48 to 36 and 24 h leads to a amorphous phase [see the XRD pattern of the powders (48 and 24 h reaction time) in the Supporting Information]. Therefore, we assume that, in the course of the 48 h long reaction, the amorphous intermediates redissolve in benzyl alcohol and finally recrystallize to anatase, which is the next dense and stable phase of TiO_2. Omnipresent in synthetic biomineralization and aqueous synthesis (38), transformation into a more stable phase in contact with a nonaqueous solvent via dissolution−recrystallization was also recently reported for nanosized ternary oxides (39). The crystallization process, following the kinetic pathway, proceeds by sequential precipitation according to Ostwald's step rule. This case illustrates the dissolution−recrystallization mechanisms of TiO_2 from titanium isopropoxide as the precursor only in benzyl alcohol and not for all nonaqueous TiO_2 routes. However, here a clear distinction between nonaqueous and aqueous synthesis of TiO_2 can be drawn. In a pure aqueous medium, isopropoxide as the precursor leads to an amorphous solid and the solid−solid transformation to the crystalline phase is usually performed by thermal treatment at elevated temperatures (39−42). Alternatively, in order to obtain directly a crystalline form in an aqueous medium, the reaction has to be performed in the presence of a base or an acid (24, 43, 44).

The crystal diameters slightly increase with an increase in the MPS concentration (see Table 1). Intuitively, one would expect that a higher surfactant concentration hinders the growth of the TiO_2 nanocrystals because of a higher adsorbance rate. In order to understand the observed experimental data, one has to consider some peculiarities of the nanocrystal nucleation process (45). In the absence of Ostwald ripening, the nanocrystals grow until the whole molecular precursor is consumed. The total amount of consumed monomer can be assumed to be constant in all reactions. The final particle size is affected by the rates of nucleation and growth, as illustrated in Figure 4. Low silane concentration leads to fast nucleation, which yields small particles and a high particle concentration. High silane concentration leads to slow nucleation and a low concentration of seeds consuming the same amount of monomer and results in large particles.

Surface Modification of TiO_2 Nanoparticles and Their Dispersion Behavior in Nonpolar Media. Organic groups attached to the surface of nanoparticles determine their dispersion behavior, which will be discussed in the following in detail. The DRIFT spectra of surface-modified TiO_2 nanoparticles are shown in Figure 5. At the surface of anatase particles prepared in the absence of silane, absorptions assigned to the OH groups and adsorbed water (stretching vibrations at 3600−3000 cm^{-1} and a deformation vibration at 1650 cm^{-1}) and to trace amounts of benzyl alcoholate (phenyl ring vibrations: ν(C−H) at 3069 and 3020 cm^{-1}, combination vibrations, multiple bands of similar intensity at 1956, 1868, 1811, and 1740 cm^{-1}, ν(C−C) at 1641 and 1600 cm^{-1}, δ(C−H) in-plane at 1207 cm^{-1}, and δ(C−H) out-of-plane at 903 cm^{-1}) were observed besides the strong Ti−O−Ti vibrations (at 790 cm^{-1}) (46).

At the surface of MPS in situ functionalized powders, there are significantly less hydroxyl groups but more benzyl alcoholate species compared to the nonfunctionalized powders. New strong bands appear corresponding to the vibrations of ν(C−H) at 2963, 2929, and 2878 cm^{-1}, ν(Si−O−C) at 1075 cm^{-1}, and ν(Si−O−Ti) at 930 cm^{-1} (46−48). Further assignment of the bands in the range below 1300 cm^{-1} is equivocal because of the strong overlap between ν(C−O) of methoxy Si−O−CH_3 at 1240−1160 cm^{-1}, γ(C−H_3) at 1250−800 cm^{-1}, symmetric ν(Si−O−Si) at 800−820 cm^{-1}, and asymmetric ν(Si−O−Si) at 1180−1250 cm^{-1} (48). Different from a previously reported postfunctionalization procedure using MPS, the spectrum does not show any evidence for the carbonyl group [ν(C═O) at 1720−1730 cm^{-1}] and the vinyl group [ν(C═C) in −CH═CH_2 at 1650 cm^{-1}], which are usually characteristic for MPS (20). This finding suggests that the MPS molecules presumably undergo an esterification reaction under the relatively harsh reaction conditions of 190 °C. The carbonyl group of MPS reacts with benzyl alcohol, resulting in the removal of carbonyl and vinyl groups from the MPS ligand, and therefore these two groups are not visible in the IR spectrum. The

Table 1. Dispersion Behavior of Differently Functionalized TiO_2 Particles in Xylene and Dichloromethane

	molar ratio titanium isopropoxide: silane	solvent	concn [wt %]	average diameter[c] [nm]	agglomerate size range [nm]	appearance	compatibility with PMMA
no	1:0			14.0		cloudy	
MPS[a]	1:0.10	xylene	0.4	15.7		cloudy	
	1:0.06	xylene	0.4	15.0	16.2–40.2	transparent	good
	1:0.02	xylene	0.4	10.5	10.0–39.9	transparent	good
TMOS	1:0.10	dichloromethane	1.2	14.6	12.0–20.2	transparent	poor
	1:0.02	dichloromethane	1.2	13.3		cloudy	
	1:0.10[b]	dichloromethane	1.2	14.6	12.2–20.1	transparent	good

[a] Postfunctionalized with oleic acid. [b] Postfunctionalized with TMOS. [c] Based on Scherrer analysis of the (101) peak.

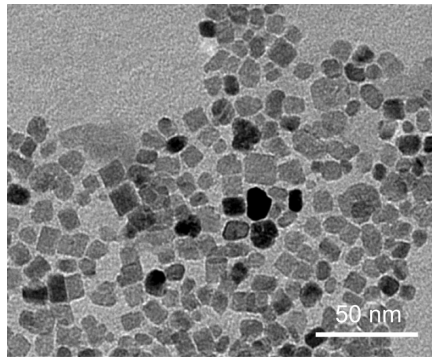

FIGURE 2. TEM image of MPS in situ functionalized particles.

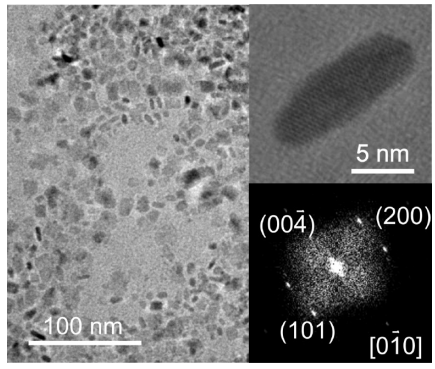

FIGURE 3. TEM image of TMOS in situ functionalized particles. Inset top: HRTEM image. Inset bottom: Power spectrum.

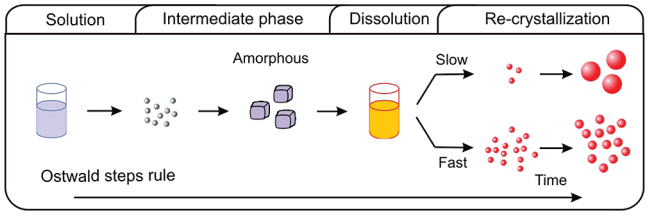

FIGURE 4. Proposed crystallization pathway for TiO_2 nanoparticles prepared from titanium isopropoxide and benzyl alcohol in the presence of silanes (for details, see the text).

remaining expected silicon species is possibly (trimethoxysilyl)propanol (49).

The substitution of TiOH groups by silyl groups was also monitored during in situ functionalization with trimethoxy(7-octen-1-yl)silane (TMOS). The broad band assigned to the hydrogen-bonded OH groups decreases, and the bands corresponding to the silane molecule vibrations appear (C—H at 2850 and 2925 cm^{-1}, C═C at 1650 cm^{-1}, asymmetric

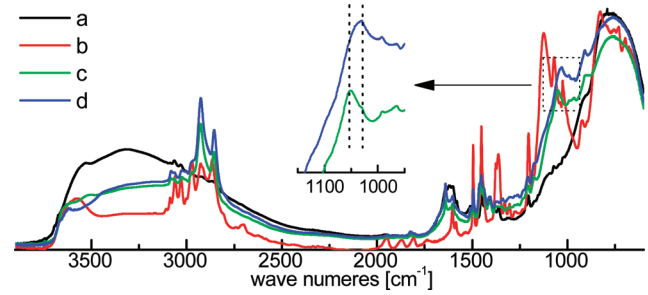

FIGURE 5. DRIFT spectra of titania powders: (a) not functionalized; (b) in situ functionalized with MPS; (c) in situ functionalized with TMOS; (d) postfunctionalized with TMOS recorded at room temperature under vacuum with KBr as the reference.

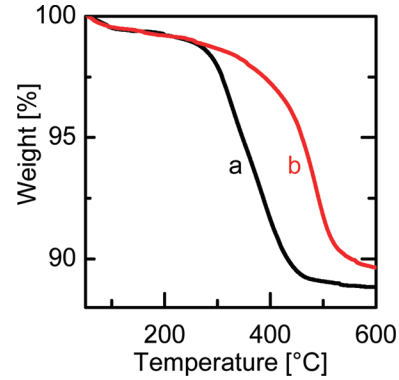

FIGURE 6. TGA measurements of TiO_2 powders under air (a) in situ and (b) postfunctionalized with TMOS.

Si—O—Si at 1050 cm^{-1}, and Si—O—Ti at 930 cm^{-1}) (48). Furthermore, besides the decrease of the absorption band assigned to the OH groups, there was only one qualitative difference observed in the spectrum of in situ modified TMOS and postfunctionalized TiO_2 nanoparticles. The asymmetric Si—O—Si stretching band shifts after postfunctionalization to the lower wavenumber 1030 cm^{-1}. The measured C, H, and N values were equal to C 10.55%, H 1.48%, and N 0.05% for in situ functionalized powders and C 9.59%, H 1.44%, and N 0.03% for postfunctionalized powders. Thermogravimetric analysis (TGA) indicates that the amount of organic groups attached to the surface during in situ functionalization and postfunctionalization corresponds to 12.4% for in situ and 11.1% for postfunctionalization with respect to the inorganic phase. The experiments (from the synthesis through postfunctionalization and finally characterization) were repeated twice, and almost the same results were obtained. Furthermore, the overall weights of C, H, and N

correspond to the weights of the volatile organics obtained from TGA experiments. However, at the same time, the maximum decomposition rate shifts to higher temperatures. This suggests that the TMOS molecules are firmly bound to the surface of nanoparticles. According to the elemental analysis, the difference in the C and H values between in situ and postfunctionalized powders is 0.96 and 0.04 wt %, respectively. On the basis of DRIFT measurements of powders, we also know that besides TMOS molecules also some hydroxyl groups and benzyl alcoholate species are adsorbed at the surface. Thus, stoichiometric considerations did not lead to an unambiguous result.

The only observed change in the DRIFT experiments between the two powders was the shift of the Si−O vibration to a lower wavenumber (see the inset in Figure 5). However, condensation reaction involving silane groups would shift the Si−O vibrations to a higher wavenumber (50). Therefore, a possible scenario is that during the postfunctionalization process tetramethylammonium hydroxide slightly increased the dissolution rate of silanes and not the condensation rate (51−56).

The precipitates from different functionalization reactions were redispersed in xylene and/or dichloromethane. Xylene and dichloromethane were chosen as solvents for the particle embedding into PMMA because they are known to be good solvents for PMMA and other polymers. For the fabrication of homogeneous composite films by solvent evaporation, a long-term stability of the dispersion of ca. 12 h is needed. Properties of the dispersions fulfilling this requirement are summarized in Table 1. Evaluation of the dispersion behavior was made on the basis of dynamic light scattering (DLS) measurements. The average agglomerate sizes are compared (size distribution).

Although the as-synthesized TiO_2 or MPS-functionalized nanoparticles have some organic species attached to their surfaces, they are not well dispersible in xylene or dichloromethane. After mixing the TiO_2 powders with solvents, cloudy and milky-like dispersions were obtained. None of these dispersions was either stable or transparent. Unexpectedly, in the case of low MPS to TiO_2 molar ratios (0.02:1), the addition of oleic acid, followed by one movement of shaking, led the dispersions to become transparent and stable (Table 1). For the particles synthesized by a reaction with a MPS to TiO_2 molar ratio of 0.1:1, this procedure did not yield any transparent dispersion (Table 1); i.e., the dispersions remained turbid and unstable. This suggests that the higher the MPS concentration in the reaction mixture, the larger the agglomerates in the dispersion. The DLS measurements of the dispersions confirm this finding (figures in the Supporting Information).

Nanoparticles functionalized with TMOS by either in situ or post ex situ (0.1:1 TMOS to TiO_2 molar ratio) methods are directly (without oleic acid) dispersible in xylene and dichloromethane.

Embedding of TiO_2 Nanocrystals into PMMA. The films based on MPS/oleic acid-functionalized TiO_2 nanoparticles, although transparent to human eyes, showed substantial transmission loss in the visible range of UV−vis spectra and are therefore not discussed. For fabrication of the composites, solely TiO_2 nanoparticles postfunctionalized with TMOS and with an average diameter of 14.6 nm were employed. It was observed that not only are their dispersions in xylene and dichloromethane free of larger agglomerates, but they also exhibit good compatibility with the PMMA solutions. It is worth to mentioning that even stable and transparent dispersions of TiO_2 only in situ functionalized with TMOS turned dimmish when mixed with the PMMA solution. The possible reason for this mismatch is the interaction at the inorganic−organic interface (17).

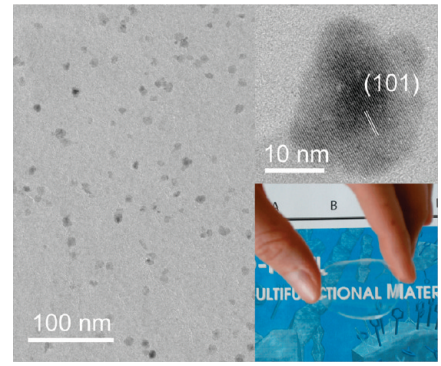

FIGURE 7. TEM image of 1.1 wt % TiO_2 in PMMA). Inset: (top) HRTEM image of single particle; (bottom) photograph of the corresponding film.

A pure PMMA film, which was produced to serve as a reference, was completely transparent. The other films were fabricated with different fractions of TiO_2 nanoparticles up to 10% (w/w). On the basis of the char yields from the TGA measurements, the titania contents in the composite films were determined as 1.1, 3.6, 6.4, and 9.3% (w/w). The values vary by 5−20% from the expected values because of the uncertainty of the mass determination of the wet powder used in the preparation of the dispersion. Because the maximum concentration of TiO_2 in PMMA is lower than 10% (w/w), it is expected that the refractive index of the composites will not significantly differ from the value of pure PMMA and therefore it is not further discussed here (1, 57).

We aimed at obtaining transparent composite films that absorb UV radiation up to the proximity of visible wavelengths with a very pronounced absorption edge. A TEM image of a film containing 1.1% (w/w) TiO_2 (Figure 7) shows that the particles are homogeneously dispersed in the matrix; i.e., agglomerates were absent. In the HRTEM micrograph (inset top), the well-resolved (101) lattice planes of the TiO_2 platelets with a d spacing of 3.385 Å are marked. Additionally, in the bottom inset is placed a photograph of the transparent self-standing 100 μm film. Photographs and UV−vis spectra of the nanocomposite films with anatase contents between 1.1 and 9.3% (w/w) are shown in Figure 8. There is no visible clouding for all of these anatase contents. The UV−vis absorption spectra (Figure 8b,c) reveal that, in particular, the films with anatase contents up to 5% (w/w) are essentially transparent in the visible wavelength region and that the films with ca. 5−10% (w/w) absorb weakly between 400 and 500 nm. However, even the film with the lowest TiO_2 content [1.1% (w/w)] markedly absorbs

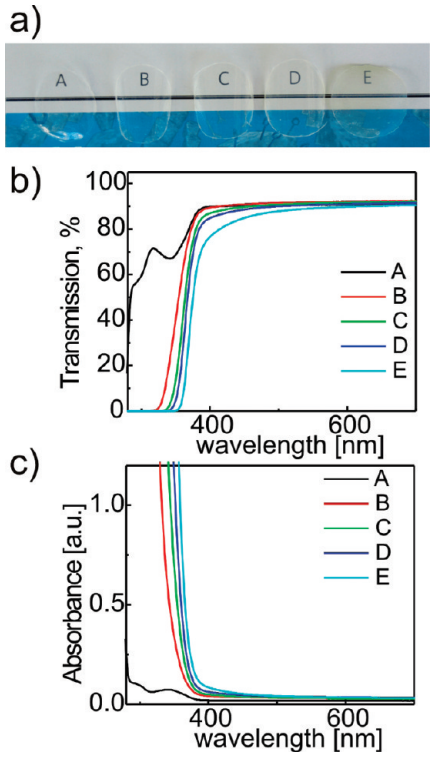

FIGURE 8. (a) Photograph of the films. UV−vis transmission (b) and absorption (c) spectra of self-supporting TiO_2−PMMA films (A−E films consisting respectively of 0.0, 1.1, 3.6, 6.4, and 9.3 wt % TiO_2 in PMMA).

UV light up to 320 nm, demonstrating good shielding efficiency even at low TiO_2 concentration. When the particle content in the matrix is raised, the absorption increases according to the law of Bouguer−Lambert−Beer. This indicates that no significant particle aggregation took place even at higher TiO_2 loading. Furthermore, the measured intensity losses correlate very well with theoretical values calculated from the Mie equation; i.e., the intensity loss value for a 1.1 wt % TiO_2 composite film at 500 nm is equal to that of the PMMA matrix alone. In fact, the theoretical intensity loss by scattering is 0.01. By variation of the particle concentrations, the UV absorption range shifts to higher wavelengths up to the close proximity of the visible region, which is important for applications in optical devices. Even for the TiO_2 content of 9.3 wt %, the visible light transmitting efficiency at a wavelength of 500 nm decreases only by about 3% compared to that of pure PMMA. The measured intensity loss at 500 nm of light agrees very well with the theoretical values, confirming very high optical transparency (see the table in the Supporting Information).

As mentioned before, the main drawback of anatase nanoparticles is their pronounced photocatalytic activity. This activity promotes the photodegradation of the PMMA matrix in the composite film and leads to transparency losses (58). Figure 9 shows a representative UV−vis absorption spectrum of a composite film [6.4% (w/w) anatase] before and after illumination for 1 and 8 h with a UV lamp with an intensity of 8900 $\mu W/cm^2$. Accordingly, the UV light intensity was almost 180 times higher than the maximum UV intensity in Mexico with a clear, sunny sky (50 $\mu W/cm^2$)

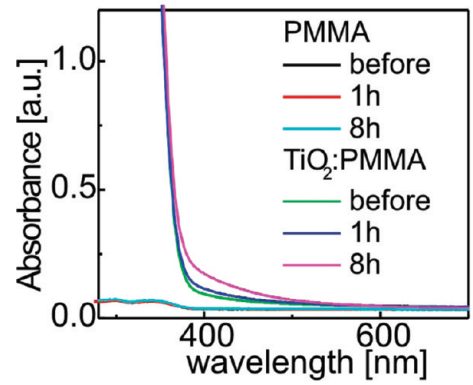

FIGURE 9. UV−vis absorption spectra of PMMA and 6 wt % TiO_2−PMMA nanocomposite films before and after illumination with a UV lamp for 1 and 8 h.

(59). For comparison, also the PMMA film was illuminated. There are no significant changes in the absorption spectrum of both pure PMMA and the composite films after 1 h of irradiation. However, after 8 h the composite films turn slightly yellow and the absorption in the visible wavelength range increases. Obviously, some degradation of the organic phase of the nanocomposites occurred (33, 34). However, the maximum transparency loss is only about 1%, which strongly suggests that the photocatalytic activity of TiO_2 was not fully, but considerably suppressed by using relatively large TiO_2 particles. The degree of polymer degradation can also be followed by the change of the C═O signal of the $-COOCH_3$ group by FTIR spectroscopy. According to reports on composites with similar quantities of anatase in PMMA and at similar UV irradiation conditions (intensity and time), the decomposition of the polymer was ≥7% (47, 60).

CONCLUSIONS

In this work, we have shown fundamental and practical aspects in the preparation of nanoparticle−polymer composite films. The goal was to optimize individually all steps including the nonaqueous synthesis, nanoparticle dispersion behavior, and incorporation of nanoparticles into the polymer matrix so that self-supporting, transparent, and UV-absorbing composites can be manufactured and basically applied in practice. The empirical optimization process of composite fabrication was supplemented by fundamental studies. It was shown that (a) crystallization follows the kinetic pathway and proceeds via the dissolution and recrystallization of anatase TiO_2 from an amorphous intermediate phase and (b) although silanes do not influence the main organic reaction mechanism, they do influence particle growth and determine the dispersibility of the nanoparticles. The gained knowledge not only is helpful in the engineering of defined properties of nanoparticles but also contributes to the basic scientific understanding of nonaqueous synthesis.

The main advantage of the nonaqueous approach combined with in situ surface functionalization with minute amounts of TMOS is that highly crystalline anatase nanoplatelets with well-defined surface composition are obtained. The as-prepared nanoparticles are easily dispersible in nonpolar media like xylene and dichloromethane. Another

technological key point is the compatibility of the dispersion with the polymer matrix. The applied postfunctionalization procedure with TMOS allows the final fine-tuning of the nanoparticles' surface and results in highly homogeneous nanocomposites. Further, it was shown that selecting an appropriate particle size minimizes both light scattering and photocatalytic activity of TiO_2 nanoparticles and therewith results in excellent transparency and UV absorption (sharp absorption edge) of the final composite films.

EXPERIMENTAL SECTION

Chemicals. Anhydrous benzyl alcohol (≥99%), titanium(IV) tetraisopropoxide (99.99%), 3-(trimethoxysilyl)propyl methacrylate (MPS; 98%), trimethoxy(7-octen-1-yl)silane (TMOS; 80%), and tetramethylammonium hydroxide [25% (w/w)] in methanol solution were supplied by Sigma-Aldrich, and titanium(IV) tetraisopropoxide (98%) was supplied by Acros. Absolute ethanol (≥99%) was purchased from J. T. Baker, *p*-xylene, dichloromethane (≥99%), and oleic acid (99.0%) from Fluka, and poly(methyl methacrylate) (PMMA) PLEXIGLAS 5N from Röhm GmbH. All chemicals were used without further purification.

Synthesis and Functionalization. In a glovebox, titanium(IV) tetraisopropoxide (4.31 mL) was added to anhydrous benzyl alcohol (15.08 mL), yielding a 1:10 molar ratio. Then, a minute amount of the respective silane (MPS or TMOS; molar ratio of silane to titanium of 0.02−0.06:1) was added. The mixture was poured into a 45 mL Teflon linear, sealed in a Parr autoclave and placed in an oven at 190 °C for 1−2 days. A white precipitate formed, which was washed three times with 10 mL of absolute ethanol, each time subjected for 10 min to ultrasonification, and after centrifugation, the supernatant liquid was removed by decantation. For the preparation of dispersions, wet powders were used, whereas the particle concentration of the dispersion was calculated from the mass of 1 mL of dried sample at the end of the process. MPS in situ functionalized powders dispersed in xylene or dichloromethane were additionally stabilized with 100 μL of oleic acid. TMOS in situ functionalized powders (300 mg) were subjected to further treatment in a mixture of absolute ethanol (10 mL), tetramethylammonium hydroxide solution [25% (w/w)] in methanol (1 mL), and an excess of TMOS (636 μL) at 50 °C for 22 h. The postfunctionalized powder was washed twice in absolute ethanol (10 mL), each time subjected for 10 min to ultrasonification, separated by centrifugation and decantation. The as-prepared wet powders are readily dispersible in xylene or dichloromethane.

Composites Fabrication. A PMMA solution [7.0% (v/v)] in xylene or dichloromethane was mixed with an appropriate amount of a 0.5% (v/v) TiO_2 dispersion in order to obtain a composite, 100 μm thick film containing 1−10% (w/w) TiO_2 in PMMA. After stirring, the transparent dispersions were cast in a Petri dish of 40 mm diameter. Composite self-supporting films of ca. 100 μm thickness were obtained by evaporation of dichloromethane at room temperature and xylene in an oven at 60 °C.

Characterization Techniques. Powder XRD patterns of TiO_2 nanoparticles were recorded on a PANalytical X'pert pro diffractometer in reflection mode equipped with an X-Celerator detector using Cu Kα radiation. The crystallite size was calculated from the full width at half-maximum of the (101) diffraction peak of anatase using Scherrer's equation (61); the value of the shape factor K was assumed to be 0.9. IR analyses were carried out with a Bruker Equinox 80v FTIR spectrometer equipped with Harrick Praying Mantis DRIFT (diffuse reflectance infrared Fourier transform) units. As a reference, a KBr spectrum was used. DLS analyses were performed on a Malvern Instruments Ltd., Worcestershire, U.K., Zetasizer 1000 mass spectrometer. HRTEM was performed with a Philips CM30ST microscope with a LaB_6 cathode operated at 300 kV. UV−vis absorption spectra of nanocomposite films were collected on a Perkin-Elmer Lambda 900 spectrometer with air as a reference spectrum.

The intensity loss was estimated by the equation

$$\frac{I}{I_0} = \exp\left\{-\left[\frac{3\Phi_p x r^3}{4\lambda^4}\left(\frac{n_p}{n_m} - 1\right)\right]\right\}$$

where r is the radius of the TiO_2 particles (7.3 nm), r_p the refractive index of the TiO_2 particles (2.49), r_m the refractive index of PMMA (1.5), ϕ_p the volume fraction of the nanoparticles [0.5−4.0% (v/v)], λ the wavelength (500 nm), and x the thickness of the film (100 μm) (62).

For photocatalytic degradation measurements, composite films were illuminated with a Blak-Ray 100 W UV lamp (365 nm) of an intensity of 8900 $\mu W/cm^2$ at a 25 cm distance for successive periods of 1 and 8 h.

TGA was measured with a Mettler Toledo DSC 822e or a DTA-STA-Netzsch instrument. Prior to the measurements, the TiO_2 powders were dried under vacuum (ca. 10^{-1} mbar). ^{13}C NMR spectroscopy was performed on a Bruker DPX 300 spectrometer with frequencies of 300/75.5 on samples diluted with $CDCl_3$ at a spinning rate of 20 Hz.

Acknowledgment. We thank Igor Djerdj and Bettina Ludi for TEM measurements, Inga Olliges-Stadler for NMR measurements, and Alexander Haensch for DRIFT spectroscopy measurements on powders. We made use of facilities provided by Electron Microscopy Center of the ETH Zürich (EMEZ), Switzerland.

Supporting Information Available: XRD pattern of powders, NMR data, TGA measurements of films, DLS measurements of dispersions, and theoretical calculation of the light intensity loss passing a nanocomposite film. This material is available free of charge via the Internet at http://pubs.acs.org.

REFERENCES AND NOTES

(1) Caseri, W. *Chem. Eng. Commun.* **2009**, *196*, 549–572.
(2) Holder, E.; Tessler, N.; Rogach, A. L. *J. Mater. Chem.* **2008**, *18*, 1064–1078.
(3) Innocenzi, P.; Lebeau, B. *J. Mater. Chem.* **2005**, *15*, 3821–3831.
(4) Sanchez, C.; Julian, B.; Belleville, P.; Popall, M. *J. Mater. Chem.* **2005**, *15*, 3559–3592.
(5) Nussbaumer, R. J.; Caseri, W. R.; Smith, P.; Tervoort, T. *Macromol. Mater. Eng.* **2003**, *288*, 44–49.
(6) Nakayama, N.; Hayashi, T. *J. Appl. Polym. Sci.* **2007**, *105*, 3662–3672.
(7) Sciancalepore, C.; Cassano, T.; Curri, M. L.; Mecerreyes, D.; Valentini, A.; Agostiano, A.; Tommasi, R.; Striccoli, M. *Nanotechnology* **2008**, 19.
(8) Yuwono, A. H.; Liu, B. H.; Xue, J. M.; Wang, J.; Elim, H. I.; Ji, W.; Li, Y.; White, T. J. *J. Mater. Chem.* **2004**, *14*, 2978–2987.
(9) Yuwono, A. H.; Xue, J. M.; Wang, J.; Elim, H. I.; Ji, W. *J. Electroceram.* **2006**, *16*, 431–439.
(10) Yuwono, A. H.; Xue, J. M.; Wang, J.; Elim, H. I.; Ji, W.; Li, Y.; White, T. J. *J. Mater. Chem.* **2003**, *13*, 1475–1479.
(11) Sanchez, C.; Escuti, M. J.; van Heesch, C.; Bastiaansen, C. W. M.; Broer, D. J.; Loos, J.; Nussbaumer, R. *Adv. Funct. Mater.* **2005**, *15*, 1623–1629.
(12) Suzuki, N.; Tomita, Y.; Kojima, T. *Appl. Phys. Lett.* **2002**, *81*, 4121–4123.
(13) Khanna, P. K.; Singh, N.; Charan, S. *Mater. Lett.* **2007**, *61*, 4725–4730.
(14) Wang, H. T.; Xu, P.; Meng, S.; Zhong, W.; Du, W. C.; Do, Q. G. *Polym. Degrad. Stab.* **2006**, *91*, 1455–1461.

(15) Khaled, S. M.; Sui, R.; Charpentier, P. A.; Rizkalla, A. S. *Langmuir* **2007**, *23*, 3988–3995.
(16) Scholz, S.; Kaskel, S. *J. Colloid Interface Sci.* **2008**, *323*, 84–91.
(17) Kickelbick, G. *J. Sol–Gel Sci. Technol.* **2008**, *46*, 281–290.
(18) Zhang, Y.; Zhou, G. E.; Zhang, Y. H.; Li, L.; Yao, L. Z.; Mo, C. M. *Mater. Res. Bull.* **1999**, *34*, 701–709.
(19) Chau, J. L. H.; Lin, Y. M.; Li, A. K.; Su, W. F.; Chang, K. S.; Hsu, S. L. C.; Li, T. L. *Mater. Lett.* **2007**, *61*, 2908–2910.
(20) Zhou, S. X.; Garnweitner, G.; Niederberger, M.; Antonietti, M. *Langmuir* **2007**, *23*, 9178–9187.
(21) Yuwono, A. H.; Zhang, Y.; Wang, J.; Zhang, X. H.; Fan, H. M.; Ji, W. *Chem. Mater.* **2006**, *18*, 5876–5889.
(22) Brinker, C. J.; Hurd, A. J. *J. Phys. (Paris)* **1994**, *4*, 1231–1242.
(23) Matsuda, A.; Kotani, Y.; Kogure, T.; Tatsumisago, M.; Minami, T. *J. Am. Ceram. Soc.* **2000**, *83*, 229–231.
(24) Finnegan, M. P.; Zhang, H. Z.; Banfield, J. F. *Chem. Mater.* **2008**, *20*, 3443–3449.
(25) Garnweitner, G.; Antonietti, M.; Niederberger, M. *Chem. Commun.* **2005**, 397–399.
(26) Pinna, N.; Niederberger, M. *Angew. Chem., Int. Ed.* **2008**, *47*, 5292–5304.
(27) Schulz, H.; Burtscher, P.; Madler, L. *Comp. Part A: Appl. Sci. Manuf.* **2007**, *38*, 2451–2459.
(28) Garnweitner, G.; Goldenberg, L. M.; Sakhno, O. V.; Antonietti, M.; Niederberger, M.; Stumpe, J. *Small* **2007**, *3*, 1626–1632.
(29) Niederberger, M.; Garnweitner, G. *Chem.—Eur. J.* **2006**, *12*, 7282–7302.
(30) Niederberger, M.; Garnweitner, G.; Pinna, N.; Antonietti, M. *J. Am. Chem. Soc.* **2004**, *126*, 9120–9126.
(31) Zhang, Z. B.; Wang, C. C.; Zakaria, R.; Ying, J. Y. *J. Phys. Chem. B* **1998**, *102*, 10871–10878.
(32) Zayat, M.; Garcia-Parejo, P.; Levy, D. *Chem. Soc. Rev.* **2007**, *36*, 1270–1281.
(33) Gesenhues, U. *J. Polym. Degrad. Stab.* **2000**, *68*, 185–196.
(34) Woo, R. S. C.; Chen, Y.; Zhu, H.; Li, J.; Kim, J. K.; Leung, C. K. Y. *Compos. Sci. Technol.* **2007**, *67*, 3448–3456.
(35) Niederberger, M.; Garnweitner, G.; Krumeich, F.; Nesper, R.; Colfen, H.; Antonietti, M. *Chem. Mater.* **2004**, *16*, 1202–1208.
(36) Garnweitner, G.; Niederberger, M. *J. Mater. Chem.* **2008**, *18*, 1171–1182.
(37) Kumar, S.; Nann, T. *Small* **2006**, *2*, 316–329.
(38) Colfen, H.; Antonietti, M. *Angew. Chem., Int. Ed.* **2005**, *44*, 5576–5591.
(39) Zhang, L. Z.; Garnweitner, G.; Djerdj, I.; Antonietti, M.; Niederberger, M. *Chem. Asian J.* **2008**, *3*, 746–752.
(40) Madras, G.; McCoy, B. J.; Navrotsky, A. *J. Am. Ceram. Soc.* **2007**, *90*, 250–255.
(41) Zhang, H. Z.; Banfield, J. F. *J. Mater. Res.* **2000**, *15*, 437–448.
(42) Zhang, H. Z.; Banfield, J. F. *J. Phys. Chem. B* **2000**, *104*, 3481–3487.
(43) Chemseddine, A.; Moritz, T. *Eur. J. Inorg. Chem.* **1999**, 235–245.
(44) Zhang, H. Z.; Banfield, J. F. *J. Phys. Chem. C* **2007**, *111*, 6621–6629.
(45) Shevchenko, E. V.; Talapin, D. V.; Schnablegger, H.; Kornowski, A.; Festin, O.; Svedlindh, P.; Haase, M.; Weller, H. *J. Am. Chem. Soc.* **2003**, *125*, 9090–9101.
(46) Pretsch, E.; Clerc, T. *Tables of spectral data for structure determination of organic compounds*; Springer: New York, 1990.
(47) Xu, J. W.; Shi, W. F.; Gong, M.; Yu, F.; Yan, L. F. *J. Appl. Polym. Sci.* **2005**, *97*, 1714–1724.
(48) Dutoit, D. C. M.; Schneider, M.; Baiker, A. *J. Catal.* **1995**, *153*, 165–176.
(49) Max, J.-J.; Daneault, S.; Chapados, C. *Can. J. Chem.* **2002**, *80*, 113–122.
(50) Corma, A.; Perezpariente, J.; Fornes, V.; Rey, F.; Rawlence, D. *Appl. Catal.* **1990**, *63*, 145–164.
(51) Lin, K.; Wang, L.; Meng, F.; Sun, Z.; Yang, Q.; Cui, Y.; Jiang, D.; Xiao, F.-S. *J. Catal.* **2005**, *235*, 423–427.
(52) Werts, M. P. L.; Badila, M.; Brochon, C.; Hebraud, A.; Hadziioannou, G. *Chem. Mater.* **2008**, *20*, 1292–1298.
(53) Philipse, A. P.; Vrij, A. *J. Colloid Interface Sci.* **1989**, *128*, 121–136.
(54) Bourgeat-Lami, E. *J. Nanosci. Nanotechnol.* **2002**, *2*, 1–24.
(55) Rohe, B.; Veeman, W. S.; Tausch, M. *Nanotechnology* **2006**, *17*, 277–282.
(56) Brinker, C. J.; Scherer, G. W. *Sol–gel science: the physics and the chemistry of sol–gel processes*; Academic Press: New York, 1990.
(57) Zhou, S. X.; Wu, L. M. *Macromol. Chem. Phys.* **2008**, *209*, 1170–1181.
(58) Zayat, M.; Garcia-Parejo, P.; Levy, D. *Chem. Soc. Rev.* **2007**, *36*, 1270–1281.
(59) Pinedo, J. L. V.; Mireles, F. G.; Ríos, C. M.; Quirino, L. L. T.; Dávila, J. I. R. *Geofís. Int.* **2006**, *45*, 263–269.
(60) Iketani, K.; Sun, R. D.; Toki, M.; Hirota, K.; Yamaguchi, O. *J. Phys. Chem. Solids* **2003**, *64*, 507–513.
(61) Scherrer, P. *Nachr. Ges. Wiss. Goettingen, Math.-Phys.* **1918**, Klasse 98.
(62) Caseri, W. *Macromol. Rapid Commun.* **2000**, *21*, 705–722.

AM9000584